A theory and a simulation capability for the growth of a solid electrolyte interphase layer at an anode particle in a Li-ion battery

Elisha Rejovitzky, Claudio V. Di Leo, Lallit Anand*
Department of Mechanical Engineering
Massachusetts Institute of Technology
Cambridge, MA 02139, USA

January 17, 2015

Abstract

A major mechanism for electrochemical aging of Li-ion batteries is the growth of a solid electrolyte interphase (SEI) layer on the surface of anode particles, which leads to capacity fade and also results in a rise in cell resistance. We have formulated a continuum theory for the growth of an SEI layer — a theory which accounts for the generation of the attendant growth stresses. The theory has been numerically implemented in a finite-element program. This simulation capability for SEI growth is coupled with our previously published chemo-mechanical simulation capability for intercalation of Li-ions in electrode particles. Using this new combined capability we have simulated the formation and growth of an SEI layer during cyclic lithiation and delithiation of an anode particle, and predicted the evolution of the growth stresses in the SEI layer. The evolution of the stress state within the SEI layer and at the SEI/anode-particle interface for spherical- and spheroidal-shaped graphite particles is studied. This knowledge of the local interfacial stresses provides a good estimate for the propensity of potential delamination of an SEI layer from an anode particle.

Keywords: Solid electrolyte interphase (SEI), Li-ion battery, Continuum mechanics, Finite element method

1 Introduction

Li-ion batteries are slated to play an increasingly prominent role in large-scale stationary energy storage systems in renewable energy plants, as well as in power systems for sustainable electric transportation vehicles. In these applications a battery must tolerate large numbers of cycles at high rates of charge and discharge, and continue to serve its function without any degradation in performance. Much remains to be done to improve upon the performance of the current generation of Li-ion batteries to meet the desired performance levels. One of the major concerns is the mitigation of "aging" of batteries — which refers to electro-chemo-mechanical degradation, capacity fade, and power loss of the batteries.

Amongst the many mechanisms which cause aging in Li-ion batteries, a major mechanism is the formation, due to decomposition of the electrolyte, of a thin *solid electrolyte interphase* (SEI) layer on the surface of anode particles. The SEI layer is electronically insulating which prevents further decomposition of the electrolyte, but it is ionically conductive and allows the diffusion of Li ions through it. However, the formation of SEI consumes Li-ions, which competes with the desired amount of Li for intercalation in the active anode material, and this causes capacity fade. In addition, since Li-ions must diffuse through the SEI layer, the formation of a SEI layer is accompanied by an increase of cell resistance. Often, the cyclic volume changes of an anode particle during Li-ion intercalation and deintercalation can cause the SEI layer to crack, delaminate, and spall from the surface of the anode particle. New SEI is then formed on the freshly exposed particle surface, which consumes more Li-ions and causes additional capacity fade. Both the chemical and

*Tel.: +1-617-253-1635; E-mail address: anand@mit.edu

mechanical integrity of the SEI are critical to the safety and performance of Li-ion batteries (cf., e.g., Lee et al., 2007; Verma et al., 2010; Barré et al., 2013).

The purpose of this paper is to report on a new theory and a finite-element-based capability for the simulation of growth of a solid electrolyte interphase layer at an anode particle in a Li-ion battery. The theory attempts to account for the generation of stress due to the growth of a SEI layer, as well as the stress that arises due to the lithiation and delithiation of the anode particle. In the literature, the stress generated due to the growth of the SEI layer is often called "irreversible" while the stress related to the swelling/de-swelling of the anode particles during lithiation/delithiation is called "reversible."

In a recent novel paper, Mukhopadhyay et al. (2012) presented experimental measurements of the reversible and irreversible stresses during SEI formation on a thin-film graphite anode. In their experiments they used a 250 μm thick, 1 in diameter quartz substrate on which, using chemical vapor deposition (CVD) techniques, they deposited (i) a 15 nm thick Ti layer; (ii) a 200 nm thick Ni layer; and finally (iii) a 200 nm layer of c-axis oriented graphite. The Ti and Ni were deposited to act as a catalyst for graphitization and as a current collector. This multilayered plate was then assembled into an electrochemical cell which was charged and discharged under galvanostatic conditions against a Li-metal cathode to develop a SEI layer on the graphite anode. The TEM micrograph in Fig. 1, taken from Mukhopadhyay et al. (2012), shows a $\approx$ 100nm-thick SEI layer which has formed on the graphite (CVD C) anode after 50 cycles of charging and discharging. After the initial deposition of the graphite layer, as well as during electrochemical cycling during which the SEI layer was formed, Mukhopadhyay et al. measured the curvature of the plate using an array of parallel laser beams focused on the back side of the quartz substrate. The results from their experiments are schematically shown in Fig. 2:

- Fig. 2 (a) shows the undeformed quartz substrate.
- After CVD deposition of the graphite layer at 1000°C and cool-down to room temperature, the graphite contracts more than the substrate and this results in a positive curvature, Fig. 2 (b).
- At the end of the first half-cycle of charging the authors observed a reduction in the positive curvature of the plate; cf. Fig. 2 (c) relative to Fig. 2 (b). This reduction in curvature occurs due to the expansion of the graphite upon lithiation, and also due to the growth of the SEI layer.
- After the first complete lithiation/delithiation cycle, the graphite contracts to its initial delithiated state. However, the authors observed a reduction in the curvature of the plate with respect to the curvature at the beginning of the first lithiation, cf. Fig. 2 (d) relative to Fig. 2 (b). This reduction in curvature is an important indicator of the expansion strain during the growth of the SEI layer.
- At the end of the second charging half-cycle the authors observed a further decrease of curvature due to expansion of the graphite and the SEI, cf. Fig. 2 (e) relative to Fig. 2 (d).
- After the second complete lithiation/delithiation cycle, they observed an increase in curvature, cf. Fig. 2 (f) relative to Fig. 2 (e). This slight increase in curvature is driven by the contraction of the graphite, while the continued formation and expansion of the SEI layer counteracts the graphite contraction. Note that due to the growth strain in the SEI, the observed curvature at the end of the second cycle was lower than the curvature at the end of the first cycle, cf. Fig. 2 (f) relative to Fig. 2 (d).

In subsequent cycles the authors observed a steady decrease in curvature due to the formation of SEI, superimposed by cyclic curvature changes due to the lithiation/delithiation of the graphite.

From their experimental measurements of the curvature changes of their multi-layered plate, Mukhopadhyay et al. calculated the changes in *a nominal equi-biaxial stress, σ_n, in the combined graphite/SEI "film" on the quartz substrate* using the classical Stoney formula (Stoney, 1909),

$$\sigma_n = \left(\frac{1}{6} \frac{E_Q}{(1-\nu_Q)} \frac{h_Q^2}{h_G} \right) \kappa; \tag{1.1}$$

here, κ is the curvature of the plate, E_Q and ν_Q are the Young's modulus and the Poisson's ratio of the quartz substrate, and h_Q and h_G are the thicknesses of the quartz and graphite layers. Fig. 3 from their

paper shows the cyclic electrical potential which was imposed in their battery for the first 20 cycles of charging/discharging, together with the results for the nominal stress that they inferred from their curvature measurements. The stress levels corresponding to the peaks of the cyclic stress profile represent the "irreversible" stress generation due to the growth of the SEI layer, while the stress levels during cycling represent the "reversible" stress due to lithiation and delithiation. Fig. 3 shows that in the course of 20 charge/discharge cycles the initially high $\sim 0.9\,\mathrm{GPa}$ tensile nominal-stress, which is introduced due to the deposition of the graphite on the quartz, reduces by a factor of two to $\sim 0.4\,\mathrm{GPa}$ due to the growth of the SEI and the attendant generation of compressive stresses in this layer. Reversible stresses in anodes due to lithiation/delithiation have been extensively addressed in the literature — however, to the best of our knowledge, Mukhopadhyay et al. are the first group to report on experimental measurements of "irreversible" stresses due to growth of SEI on an anode.

As mentioned above, the purpose of this paper is to report on our new continuum-mechanical theory and a finite-element-based capability for the simulation of growth of a solid electrolyte interphase layer at an anode particle in a Li-ion battery. In formulating our theory we attempt to account for (i) the stress generation due to the lithiation and delithiation of anode particles, and (ii) the stress-generation due to the growth of an SEI layer. We also report on the results from the use of our theory for:

1. A study of the problem of SEI formation on the surface of a flat anode undergoing cyclic lithiation and delithiation, as in the study of Mukhopadhyay et al. (2012). We demonstrate that we can reproduce their experimental results with reasonable *quantitative* accuracy.

2. A study of the problem of SEI formation on the surface of spherical and spheroidal graphite particles undergoing cyclic lithiation and delithiation. The stress state in the SEI layer and at the SEI-particle interface are calculated and the propensity of potential delamination of the SEI layer from the particle is identified. We show that the interplay between reversible particle swelling/deswelling and irreversible SEI growth has a crucial effect on the magnitude of the stress levels that are generated, and consequently on the mechanical integrity of the SEI layer.

2 Modeling of lithiation/delithiation of anode particles

In order to properly simulate the growth of an SEI layer on the surface of an anode particle of a Li-ion battery, we must of course account for the chemo-mechanical deformation during charging and discharging of the anode itself — a process during which commonly used anode materials undergo substantial volume changes. As we shall show, such volumetric changes of an anode particle can have a significant effect on the stress distribution that is developed within the SEI layer. In order to model the intercalation of Li in an anode we will use our recently published theory for species diffusion coupled with large elastic deformations (Di Leo et al., 2014). Since this Li intercalation theory is not the main subject of the present paper, we defer a brief summary of this theory to Section 6, and in the next section we turn our attention to the main subject, viz., modeling the growth of an SEI layer.

3 Modeling of SEI growth

The process of growth of an SEI layer involves the addition of new mass onto the surface of an anode particle which is accompanied by a growth strain in the SEI — as a result, the newly-deposited SEI layer and the anode contain balanced residual stresses. Although the deposition of the layer and the associated strain generation occur simultaneously, we conceptually *idealize* the growth of an SEI layer on a surface of interest as a *two-step process* shown schematically in Fig. 4:

- The first step, which we refer to as **deposition**, results in the formation of a **strain-free** layer of SEI on the surface of interest, cf. Fig. 4 (a) to (b). This process controls the rate of increase of the thickness of the SEI layer perpendicular to the surface of interest.

- The second step, which we refer to as **in-plane expansion**, models the evolution of strain mismatch between the SEI layer and the substrate, cf. Fig. 4 (b) to (c). *Note that the reference configuration for the start of the expansion process is the "strain-free" layer created during the deposition step.*

Taken together, this idealized two-step process serves to model the experimentally observed growth of a SEI layer on a substrate.

In the next two sections we detail the theory and the numerical modeling of each of these two conceptually-separated sub-processes.

Remark. The intrinsic mechanism for the growth strains in the SEI and the attendant large growth stresses (of the order of -1 GPa) is not completely clear. Based on their recent experimental study on the chemical and morphological changes, and stress generation during SEI formation on c-axis oriented graphitic carbon electrodes, Tokranov et al. (2014) have suggested that it is the disruption of the surface of the graphite caused by solvated ions during the initial stages of formation of the SEI which is the dominant cause of stress at high potentials (above 0.5 V).

Our continuum model for SEI growth does not explicitly account for any specific mechanism for the formation and growth of the SEI. Rather, it assumes only that SEI formation occurs and is accompanied by growth strains which can results in stress generation at the SEI/anode interface.

□

4 Numerical modeling of SEI deposition

Fig. 5 shows a schematic of our numerical simulation scheme for modeling the deposition of an SEI layer by the sequential conversion of multiple layers of finite elements — from elements with properties representing the electrolyte, to elements with properties representing the SEI. Fig. 5(a) shows three rows of elements representing the electrolyte (colored blue) adjacent to three rows of elements representing the graphite (colored gray); the electrolyte elements are sequentially converted to strain-free SEI elements (colored pink) at three prescribed times $(t^{(1)}_{\text{dep}}, t^{(2)}_{\text{dep}}, t^{(3)}_{\text{dep}})$. Fig. 5 (b) shows the resulting profile of the total SEI layer thickness h versus time t. In our numerical simulations we will choose the conversion times $t \in [t^{(1)}_{\text{dep}}, t^{(2)}_{\text{dep}}, t^{(3)}_{\text{dep}}, \ldots, t^{(N)}_{\text{dep}}]$ for the different electrolyte layers so that the resulting thickness $h(t)$ of the total SEI layer approximates the experimentally-observed square-root growth profile (Smith et al., 2011). That is, we will choose the times when the electrolyte layers convert to SEI such that SEI total thickness growth approximates

$$h(t) \propto \sqrt{t}. \tag{4.1}$$

We emphasize that this square-root growth profile is something that we shall prescribe — it is not an outcome of a diffusion-controlled chemical reaction model.

The electrolyte is modeled as a linear elastic material with a very low Young's modulus of $E = 0.5\,\text{MPa}$, and a zero-valued Poisson's ratio, $\nu = 0$. Thus, any deformation of the graphite/electrolyte system produces stresses in the graphite which are essentially unaffected by the presence of the electrolyte elements. The specific constitutive behavior of the newly-formed strain-free SEI layer for times $t > t_{\text{dep}}$ is described in the next section.

Prior to the conversion of an electrolyte element to an SEI element, that is for $t < t_{\text{dep}}$, the standard deformation gradient $\mathbf{F}(t)$ is used for the constitutive calculations for an electrolyte element. The stress-free reference configuration for an SEI element of interest is its configuration at the time $t = t_{\text{dep}}$, when it is first converted from an element representing electrolyte to an element representing SEI. Thus, to model the subsequent in-plane expansion of a newly-deposited SEI element, the appropriate deformation gradient that is to be used for constitutive calculations is the *relative deformation gradient*,

$$\mathbf{F}_{\text{SEI}}(\tau) \stackrel{\text{def}}{=} \mathbf{F}_{t_{\text{dep}}}(\tau) = \mathbf{F}(\tau)\mathbf{F}(t_{\text{dep}})^{-1} \qquad \text{for } \tau > t_{\text{dep}}. \tag{4.2}$$

5 Modeling of in-plane expansion of SEI

In this section we detail our constitutive theory for modeling the in-plane expansion of the SEI layer once it has been deposited on the surface of an anode. This theory is based — in major part — on the theory of "growing matter in living systems" (cf., e.g., Kuhl, 2014, for a recent review of the substantial literature on this topic), which employs the widely-used Kroner (1960)-Lee (1969) multiplicative decomposition of the deformation gradient,

$$\mathbf{F} = \mathbf{F}^e\mathbf{F}^g. \tag{5.1}$$

Here, for modeling the in-plane expansion of the SEI,

- The deformation gradient in (5.1) is to be interpreted as the deformation gradient $\mathbf{F}_{\rm SEI}$ defined in (4.2),
$$\mathbf{F} \equiv \mathbf{F}_{\rm SEI}. \tag{5.2}$$
- Also, we shall take $\mathbf{F}^g$ to be of the specific form given in eq. (5.12), which restricts the "growth" to an in-plane expansion (more on this below).

For economy of notation we shall continue to use the standard notation in (5.1), with the understanding that the deformation gradient $\mathbf{F}$ in what follows in this section is $\mathbf{F}_{\rm SEI}$, and that $\mathbf{F}^g$ will have the form (5.12), so that the "growth" represented by $\mathbf{F}^g$ refers only to in-plane expansion of the SEI.

5.1 Kinematics

We denote by B the reference configuration for the SEI. An arbitrary material point of B is denoted by $\mathbf{X}$, and a *motion* of B is a smooth one-to-one mapping $\mathbf{x} = \boldsymbol{\chi}(\mathbf{X}, t)$ with *deformation gradient*, *velocity*, and *velocity gradient* given by[1]

$$\mathbf{F} = \nabla\boldsymbol{\chi}, \qquad \mathbf{v} = \dot{\boldsymbol{\chi}}, \qquad \mathbf{L} = \operatorname{grad}\mathbf{v} = \dot{\mathbf{F}}\mathbf{F}^{-1}. \tag{5.3}$$

Following modern developments of large-deformation plasticity theory (cf., e.g., Gurtin et al., 2010) and growth theory (cf., e.g., Kuhl, 2014), we base our theory on the multiplicative decomposition (5.1) of the deformation gradient. Where, suppressing the argument t:

(i) $\mathbf{F}^g(\mathbf{X})$ represents the local distortion of the material neighborhood of $\mathbf{X}$ due to growth; and

(ii) $\mathbf{F}^e(\mathbf{X})$ represents the subsequent stretching and rotation of this coherent but distorted material neighborhood, and thereby represents a corresponding elastic distortion.

We refer to $\mathbf{F}^g$ and $\mathbf{F}^e$ as the *growth and elastic distortions*, respectively, and we refer to the local space at $\mathbf{X}$ represented by the range of $\mathbf{F}^g(\mathbf{X})$, as the *intermediate space* at $\mathbf{X}$.

As is standard, we assume that

$$J \stackrel{\rm def}{=} \det\mathbf{F} > 0, \tag{5.4}$$

and hence, using (5.1),

$$J = J^eJ^g, \qquad \text{where} \qquad J^e \stackrel{\rm def}{=} \det\mathbf{F}^e > 0 \qquad \text{and} \qquad J^g \stackrel{\rm def}{=} \det\mathbf{F}^g > 0, \tag{5.5}$$

so that $\mathbf{F}^e$ and $\mathbf{F}^g$ are invertible.

The right polar decomposition of $\mathbf{F}^e$ is given by

$$\mathbf{F}^e = \mathbf{R}^e\mathbf{U}^e, \tag{5.6}$$

[1]Notation: We use standard notation of modern continuum mechanics Gurtin et al. (2010). Specifically: ∇ and Div denote the gradient and divergence with respect to the material point $\mathbf{X}$ in the reference configuration; grad and div denote these operators with respect to the point $\mathbf{x} = \boldsymbol{\chi}(\mathbf{X}, t)$ in the deformed body; a superposed dot denotes the material time-derivative. Throughout, we write $\mathbf{F}^{e-1} = (\mathbf{F}^e)^{-1}$, $\mathbf{F}^{e-\top} = (\mathbf{F}^e)^{-\top}$, etc. We write $\operatorname{tr}\mathbf{A}$, $\operatorname{sym}\mathbf{A}$, $\operatorname{skw}\mathbf{A}$, $\mathbf{A}_0$, and $\operatorname{sym}_0\mathbf{A}$ respectively, for the trace, symmetric, skew, deviatoric, and symmetric-deviatoric parts of a tensor $\mathbf{A}$. Also, the inner product of tensors $\mathbf{A}$ and $\mathbf{B}$ is denoted by $\mathbf{A}\!:\!\mathbf{B}$, and the magnitude of $\mathbf{A}$ by $|\mathbf{A}| = \sqrt{\mathbf{A}\!:\!\mathbf{A}}$.

where $\mathbf{R}^e$ is a rotation, while $\mathbf{U}^e$ is a symmetric, positive-definite tensor with

$$\mathbf{U}^e = \sqrt{\mathbf{F}^{e\top}\mathbf{F}^e}. \tag{5.7}$$

As is standard, we define the elastic right Cauchy-Green tensor by

$$\mathbf{C}^e = \mathbf{U}^{e2} = \mathbf{F}^{e\top}\mathbf{F}^e. \tag{5.8}$$

By $(5.3)_3$ and (5.1),

$$\mathbf{L} = \mathbf{L}^e + \mathbf{F}^e\mathbf{L}^g\mathbf{F}^{e-1}, \tag{5.9}$$

with

$$\mathbf{L}^e = \dot{\mathbf{F}}^e\mathbf{F}^{e-1}, \qquad \mathbf{L}^g = \dot{\mathbf{F}}^g\mathbf{F}^{g-1}. \tag{5.10}$$

We define the elastic and growth stretching and spin tensors through

$$\left.\begin{aligned} \mathbf{D}^e &= \operatorname{sym}\mathbf{L}^e, \qquad \mathbf{W}^e = \operatorname{skw}\mathbf{L}^e, \\ \mathbf{D}^g &= \operatorname{sym}\mathbf{L}^g, \qquad \mathbf{W}^g = \operatorname{skw}\mathbf{L}^g, \end{aligned}\right\} \tag{5.11}$$

so that $\mathbf{L}^e = \mathbf{D}^e + \mathbf{W}^e$ and $\mathbf{L}^g = \mathbf{D}^g + \mathbf{W}^g$.

Since an increase in thickness of the SEI layer in a direction perpendicular to the anode surface does not result in generation of "growth stresses", we have modeled SEI growth as two separate processes (cf. Section 3): (a) deposition, which results in a stress-free increase in thickness, and (b) area growth which gives rise to growth stresses because of the constraint of the substrate. Accordingly, we make the following additional kinematical assumptions concerning SEI growth. Let $\Pi_{\mathrm{R}}(\mathbf{X})$ denote a plane through an infinitesimal neighborhood of $\mathbf{X}$ on the surface of the anode oriented by a unit normal vector $\mathbf{m}_{\mathrm{R}}(\mathbf{X})$. Then, as a specific model for $\mathbf{F}^g$ we consider *isotropic area growth*, described by

$$\mathbf{F}^g = \mathbf{m}_{\mathrm{R}} \otimes \mathbf{m}_{\mathrm{R}} + \lambda^g_{\perp}\,(\mathbf{1} - \mathbf{m}_{\mathrm{R}} \otimes \mathbf{m}_{\mathrm{R}}), \tag{5.12}$$

where $\lambda^g_{\perp}$ represents the *growth stretch* in the plane Π_{R} perpendicular to $\mathbf{m}_{\mathrm{R}}$. Futher, we define

$$\epsilon^g_{\perp} \stackrel{\text{def}}{=} \ln \lambda^g_{\perp}, \tag{5.13}$$

as a corresponding *growth strain*, and introduce an

$$\textit{area growth ratio } \Theta^g,$$

which represents the ratio of the area normal to $\mathbf{m}_{\mathrm{R}}$ in the intermediate configuration to the area normal to $\mathbf{m}_{\mathrm{R}}$ in the reference configuration. Due to our assumption of pure in-plane growth, Θ^g is identically equal to J^g and related to $\lambda^g_{\perp}$ as follows:

$$\Theta^g \equiv J^g = (\lambda^g_{\perp})^2. \tag{5.14}$$

Thus, note that

$$\dot{\Theta}^g = 2\Theta^g\dot{\epsilon}^g_{\perp}. \tag{5.15}$$

Since,

$$\dot{\mathbf{F}}^g = \dot{\lambda}^g_{\perp}\,(\mathbf{1} - \mathbf{m}_{\mathrm{R}} \otimes \mathbf{m}_{\mathrm{R}}), \tag{5.16}$$

and

$$\mathbf{F}^{g-1} = \mathbf{m}_{\mathrm{R}} \otimes \mathbf{m}_{\mathrm{R}} + \frac{1}{\lambda^g_{\perp}}(\mathbf{1} - \mathbf{m}_{\mathrm{R}} \otimes \mathbf{m}_{\mathrm{R}}), \tag{5.17}$$

using $(5.10)_2$, (5.17), and (5.13) we obtain

$$\mathbf{L}^g = \dot{\epsilon}^g_{\perp}\,(\mathbf{1} - \mathbf{m}_{\mathrm{R}} \otimes \mathbf{m}_{\mathrm{R}}). \tag{5.18}$$

Upon using (5.15) in (5.18) gives

$$\mathbf{L}^g = (\dot{\Theta}^g\Theta^{g-1})\,\mathbf{S}^g, \tag{5.19}$$

where

$$\mathbf{S}^g \stackrel{\text{def}}{=} \frac{1}{2}(\mathbf{1} - \mathbf{m}_{\text{R}} \otimes \mathbf{m}_{\text{R}}). \tag{5.20}$$

We restrict attention to circumstances in which

$$\dot{\Theta}^g \geq 0, \tag{5.21}$$

so that in-plane growth is *irreversible*. Note that $\mathbf{L}^g$ is symmetric, so that

$$\mathbf{L}^g \equiv \mathbf{D}^g, \tag{5.22}$$

and

$$\mathbf{W}^g = \mathbf{0}. \tag{5.23}$$

5.2 Free energy imbalance

Introducing the Helmholtz free energy ψ_{R} per unit reference volume, the classical local free-energy imbalance under isothermal conditions is (Gurtin et al., 2010),

$$\dot{\psi}_{\text{R}} - \mathbf{T}_{\text{R}} : \dot{\mathbf{F}} \leq 0\,, \tag{5.24}$$

where, with $\mathbf{T}_{\text{R}}$ denoting the standard Piola stress, the term $\mathbf{T}_{\text{R}} : \dot{\mathbf{F}}$ in (5.24) represents the stress-power per unit reference volume.

Recall that the Piola stress $\mathbf{T}_{\text{R}}$ is related to the symmetric Cauchy stress $\mathbf{T}$ by

$$\mathbf{T}_{\text{R}} = J\,\mathbf{T}\,\mathbf{F}^{-\top}. \tag{5.25}$$

Thus, using (5.1), $(5.10)_2$, (5.14), and (5.25), the stress-power may be written as

$$\begin{aligned}
\mathbf{T}_{\text{R}} : \dot{\mathbf{F}} &= \mathbf{T}_{\text{R}} : (\dot{\mathbf{F}}^e \mathbf{F}^g + \mathbf{F}^e \dot{\mathbf{F}}^g), \\
&= (\mathbf{T}_{\text{R}} \mathbf{F}^{g\top}) : \dot{\mathbf{F}}^e + (\mathbf{F}^{e\top} \mathbf{T}_{\text{R}}) : \dot{\mathbf{F}}^g, \\
&= \Theta^g \left((J^e \mathbf{F}^{e-1} \mathbf{T} \mathbf{F}^{e-\top}) : (\mathbf{F}^{e\top} \dot{\mathbf{F}}^e) + (\mathbf{C}^e J^e \mathbf{F}^{e-1} \mathbf{T} \mathbf{F}^{e-\top}) : \mathbf{L}^g \right).
\end{aligned} \tag{5.26}$$

In view of (5.26), we introduce two new stress measures:

- The elastic second Piola stress,

$$\mathbf{T}^e \stackrel{\text{def}}{=} J^e \mathbf{F}^{e-1} \mathbf{T} \mathbf{F}^{e-\top}, \tag{5.27}$$

  which is *symmetric* on account of the symmetry of the Cauchy stress $\mathbf{T}$.

- The Mandel stress,

$$\mathbf{M}^e \stackrel{\text{def}}{=} \mathbf{C}^e \mathbf{T}^e, \tag{5.28}$$

  which in general is *not symmetric*.

Further, from (5.8)

$$\dot{\mathbf{C}}^e = \dot{\mathbf{F}}^{e\top} \mathbf{F}^e + \mathbf{F}^{e\top} \dot{\mathbf{F}}^e\,. \tag{5.29}$$

Thus, using the definitions (5.27), (5.28) and the relation (5.29), the stress-power (5.26) may be written as

$$\mathbf{T}_{\text{R}} : \dot{\mathbf{F}} = \Theta^g \left(\tfrac{1}{2} \mathbf{T}^e : \dot{\mathbf{C}}^e + \mathbf{M}^e : \mathbf{L}^g \right). \tag{5.30}$$

Using (5.30) in (5.24), and using (5.19) allows us to write the free energy imbalance as

$$\dot{\psi}_{\text{R}} - \Theta^g \big(\tfrac{1}{2} \mathbf{T}^e : \dot{\mathbf{C}}^e \big) - \dot{\Theta}^g \mathbf{M}^e : \mathbf{S}^g \leq 0\,. \tag{5.31}$$

Remark. For brevity we have not discussed invariance properties of the various fields appearing in our theory. However, such considerations are straight-forward and extensively elaborated upon in the context of plasticity theories, which have a similar structure, by Gurtin et al. (2010). Here, we simply note that all quantities in the free energy imbalance (5.31) are invariant under a change in frame. □

5.3 Energetic constitutive equations

Guided by the free-energy imbalance (5.31), we first consider the following set of constitutive equations for the free energy $\psi_{\rm R}$ and the stress $\mathbf{T}^e$:

$$\left.\begin{aligned}\psi_{\rm R} &= \bar{\psi}_{\rm R}(\mathbf{C}^e, \Theta^g),\\ \mathbf{T}^e &= \bar{\mathbf{T}}^e(\mathbf{C}^e, \Theta^g).\end{aligned}\right\} \tag{5.32}$$

Substituting the constitutive equations (5.32) into the dissipation inequality, we find that the free-energy imbalance (5.31) may then be written as

$$\Big(\frac{\partial\bar{\psi}_{\rm R}(\mathbf{C}^e,\Theta^g)}{\partial\mathbf{C}^e} - \Theta^g\left(\tfrac{1}{2}\,\bar{\mathbf{T}}^e(\mathbf{C}^e,\Theta^g)\right)\Big):\dot{\mathbf{C}}^e - \left(-\frac{\partial\bar{\psi}_{\rm R}(\mathbf{C}^e,\Theta^g)}{\partial\Theta^g} + \mathbf{M}^e:\mathbf{S}^g\right)\dot{\Theta}^g \le 0\,. \tag{5.33}$$

This inequality is satisfied provided that the free energy determines the stress $\mathbf{T}^e$ through the "state relation"

$$\mathbf{T}^e = \Theta^{g-1}\,\left(2\frac{\partial\bar{\psi}_{\rm R}(\mathbf{C}^e,\Theta^g)}{\partial\mathbf{C}^e}\right), \tag{5.34}$$

together with the dissipation inequality

$$\mathcal{F}\dot{\Theta}^g \ge 0, \tag{5.35}$$

where

$$\mathcal{F} \stackrel{\rm def}{=} \mathcal{A} + \mathbf{M}^e:\mathbf{S}^g \tag{5.36}$$

represents a thermodynamic force conjugate to $\dot{\Theta}^g$, with

$$\mathcal{A}(\mathbf{C}^e,\Theta^g) \stackrel{\rm def}{=} -\frac{\partial\bar{\psi}_{\rm R}(\mathbf{C}^e,\Theta^g)}{\partial\Theta^g}, \tag{5.37}$$

representing an energetic constitutive contribution to $\mathcal{F}$ — called the *affinity* (cf., e.g., Loeffel and Anand, 2011).

5.4 Dissipative constitutive equation

Guided by (5.35), we presume that the area expansion rate $\dot{\Theta}^g$ is given by a constitutive equation

$$\dot{\Theta}^g = \hat{\dot{\Theta}}^g(\Theta^g,\mathcal{F}) \ge 0, \tag{5.38}$$

such that $\mathcal{F}\,\dot{\Theta}^g > 0$ holds whenever $\dot{\Theta}^g > 0$.

5.5 Specialization of the constitutive equations

5.5.1 Free energy

Next, restricting ourselves to an isotropic elastic response for the SEI, the free energy function $\bar{\psi}_{\rm R}(\mathbf{C}^e,\Theta^g)$ is taken as an isotropic function of its arguments. An immediate consequence is that the free energy function has the representation

$$\bar{\psi}_{\rm R}(\mathbf{C}^e,\Theta^g) = \breve{\psi}_{\rm R}(\mathcal{I}_{\mathbf{C}^e},\Theta^g), \tag{5.39}$$

with

$$\mathcal{I}_{\mathbf{C}^e} = \Big(I_1(\mathbf{C}^e), I_2(\mathbf{C}^e), I_3(\mathbf{C}^e)\Big)$$

the list of principal invariants of $\mathbf{C}^e$. Next, the spectral representation of $\mathbf{C}^e$ is

$$\mathbf{C}^e = \sum_{i=1}^{3}\omega_i^e\,\mathbf{r}_i^e\otimes\mathbf{r}_i^e, \qquad \text{with} \qquad \omega_i^e = {\lambda_i^e}^2, \tag{5.40}$$

where $(\mathbf{r}_1^e, \mathbf{r}_2^e, \mathbf{r}_2^e)$ are the orthonormal eigenvectors of $\mathbf{C}^e$ and $\mathbf{U}^e$, and $(\lambda_1^e, \lambda_2^e, \lambda_3^e)$ are the positive eigenvalues of $\mathbf{U}^e$. Let

$$\mathbf{E}^e \stackrel{\text{def}}{=} \ln \mathbf{U}^e = \sum_{i=1}^{3} E_i^e \, \mathbf{r}_i^e \otimes \mathbf{r}_i^e, \qquad \text{with} \qquad E_i^e \stackrel{\text{def}}{=} \ln \lambda_i^e \,, \tag{5.41}$$

denote the logarithmic elastic strain. With the logarithmic elastic strain defined by (5.41), for isotropic materials we henceforth consider a free energy of the form

$$\psi_{\text{R}} = \hat{\psi}_{\text{R}}(\mathcal{I}_{\mathbf{E}^e}, \Theta^g), \tag{5.42}$$

with $\mathcal{I}_{\mathbf{E}^e}$ a list of principal invariants of $\mathbf{E}^e$, or equivalently a list of principal values of $\mathbf{E}^e$. Then, straightforward calculations (cf., e.g., Anand and Su, 2005, Section 7.2) show that the Mandel stress is *symmetric* and given by

$$\mathbf{M}^e = \Theta^{g-1} \left(\frac{\partial \hat{\psi}_{\text{R}}(\mathcal{I}_{\mathbf{E}^e}, \Theta^g)}{\partial \mathbf{E}^e} \right), \tag{5.43}$$

and the corresponding Cauchy stress is given by

$$\mathbf{T} = J^{e-1} \mathbf{R}^e \mathbf{M}^e \mathbf{R}^{e\top}. \tag{5.44}$$

Next, we consider the free energy to be a separable function of the form

$$\hat{\psi}_{\text{R}}(\mathcal{I}_{\mathbf{E}^e}, \Theta^g) = \psi^e(\mathcal{I}_{\mathbf{E}^e}, \Theta^g) + \psi^{\text{chem}}(\Theta^g). \tag{5.45}$$

Here:

(i) ψ^e is an elastic energy given by

$$\psi^e(\mathcal{I}_{\mathbf{E}^e}, \Theta^g) = \Theta^g \underbrace{\left(\tfrac{1}{2}\mathbf{E}^e : \mathbb{C}\mathbf{E}^e\right)}_{\psi_0^e}, \qquad \mathbb{C} \stackrel{\text{def}}{=} 2G\mathbb{I} + \Big(K - \frac{2}{3}G\Big)\mathbf{1} \otimes \mathbf{1}, \tag{5.46}$$

where $\mathbb{C}$ is the elasticity tensor, with $\mathbb{I}$ and $\mathbf{1}$ the fourth- and second-order identity tensors, and the parameters

$$G > 0, \qquad K > 0, \tag{5.47}$$

are the shear modulus and bulk modulus, respectively. The term ψ_0^e in (5.46) is an elastic energy measured per unit volume of the intermediate space; multiplication by Θ^g converts it to an energy measured per unit volume of the reference space. This is a simple generalization of the classical strain energy function of infinitesimal isotropic elasticity to moderately large elastic strains (Anand, 1979, 1986).

(ii) ψ^{chem} is a chemical energy related to the SEI reaction. We assume the following simple linear relation (cf., e.g., Loeffel and Anand, 2011)

$$\psi^{\text{chem}} = H(1 - \Theta^g), \tag{5.48}$$

where the parameter $H > 0$ represents a *chemistry modulus*. Thus, as Θ^g increases from unity the free-energy decreases, which implies that area growth is energetically favorable.

Thus

$$\psi_{\text{R}} = \Theta^g \left[\tfrac{1}{2}\mathbf{E}^e : \mathbb{C}\mathbf{E}^e\right] + H(1 - \Theta^g). \tag{5.49}$$

Then, by (5.43), (5.37), and (5.46), the Mandel stress and the affinity are given by

$$\begin{aligned} \mathbf{M}^e &= \mathbb{C}\mathbf{E}^e = 2G\mathbf{E}_0^e + K(\text{tr}\,\mathbf{E}^e)\mathbf{1}, \\ \mathcal{A} &= H - \left[\tfrac{1}{2}\mathbf{E}^e : \mathbb{C}\mathbf{E}^e\right]. \end{aligned} \tag{5.50}$$

Using $(5.50)_1$, (5.44), and (5.41) the Cauchy stress $\mathbf{T}$ is given by

$$\mathbf{T} = J^{e-1} \left(2G\mathbf{E}_{\text{H}}^e + (K - (2/3)G)(\text{tr}\ \mathbf{E}_{\text{H}}^e)\mathbf{1}\right) \qquad \text{with} \qquad \mathbf{E}_{\text{H}}^e \stackrel{\text{def}}{=} \mathbf{R}^e \mathbf{E}^e \mathbf{R}^{e\top}, \tag{5.51}$$

where $\mathbf{E}_{\text{H}}^e$ is Hencky's spatial logarithmic strain.

Also, from $(5.50)_2$ and (5.36) the "driving force" $\mathcal{F}$ for $\dot{\Theta}^g$ is

$$\mathcal{F} = H + \mathbf{M}^e : \mathbf{S}^g - \tfrac{1}{2}\mathbf{E}^e : \mathbb{C}\mathbf{E}^e. \tag{5.52}$$

5.5.2 Evolution equation for Θ^g

Guided by Kuhl (2014), we choose a simple special form for (5.38),

$$\dot{\Theta}^g = \begin{cases} k\left(1 - \dfrac{\Theta^g}{\Theta^g_{\max}}\right)\mathcal{F} & \text{if } \mathcal{F} > 0, \\ 0 & \text{otherwise,} \end{cases} \tag{5.53}$$

where, $k > 0$ is a positive-valued (possibly temperature-dependent) parameter with units of $\mathrm{m}^3/(\mathrm{J}\cdot\mathrm{sec})$, and $\Theta^g_{\max}$ is the maximum area growth.

This completes the constitutive theory for modeling the in-plane expansion of the SEI.

6 Summary of a theory for lithium intercalation coupled with large elastic deformation

In order to model the diffusion of Li in the anode, and the resulting volumetric expansion/contraction of the anode due to Li intercalation, we make use of our recently published theory for species diffusion coupled with large elastic deformations (Di Leo et al., 2014). The theory of Di Leo et al. (2014) was formulated to also account for phase separation. Here we restrict our attention to a simplified version of the theory which neglects phase separation. The simplified version of the theory, using notation and terminology essentially identical to that of the previous section, is summarized below:

6.1 Constitutive equations

1. **Kinematics**. The deformation gradient is multiplicatively decomposed into an elastic distortion $\mathbf{F}^e$, and a chemical distortion $\mathbf{F}^c$ through

$$\mathbf{F} = \mathbf{F}^e\mathbf{F}^c\,, \quad J = J^eJ^c. \tag{6.1}$$

2. **Chemical distortion**. We take the chemical distortion to be spherical and to depend on the Li concentration,

$$\mathbf{F}^c = (J^c)^{1/3}\,\mathbf{1} \quad \text{with} \quad J^c = 1 + \Omega(c - c_0) > 0, \tag{6.2}$$

where Ω is a constant partial molar volume of the intercalating Li in the body, with c_0 the initial concentration.

3. **Stress**. The Mandel and Cauchy stress tensors are given by

$$\begin{aligned} &\mathbf{M}^e = 2G\mathbf{E}^e + (K - (2/3)G)(\mathrm{tr}\mathbf{E}^e)\mathbf{1}, \\ &\mathbf{T} = J^{e-1}\left(2G\mathbf{E}^e_{\mathrm{H}} + (K - (2/3)G)(\mathrm{tr}\mathbf{E}^e_{\mathrm{H}})\mathbf{1}\right), \qquad \text{with} \qquad \mathbf{E}^e_{\mathrm{H}} \stackrel{\mathrm{def}}{=} \mathbf{R}^e\mathbf{E}^e\mathbf{R}^{e\top}. \end{aligned} \tag{6.3}$$

4. **Chemical Potential**. The chemical potential of the Li in the anode is given by

$$\mu = \mu^0 + R\vartheta \ln\left(\frac{\bar{c}}{1-\bar{c}}\right) - \Omega\frac{1}{3}\mathrm{tr}\mathbf{M}^e, \tag{6.4}$$

where $\bar{c} \stackrel{\mathrm{def}}{=} c/c_{\max}$ is the normalized Li concentration, with $c_{\max}$ the maximum Li concentration, R is the gas constant, ϑ is the temperature, and μ^0 is a constant reference chemical potential. In our calculations we consider only isothermal conditions at $\vartheta = 300\mathrm{K}$.

5. **Species flux**. The flux $\mathbf{j}_{\mathrm{R}}$ of the intercalating Li is taken to be linear in the gradient of the chemical potential,

$$\mathbf{j}_{\mathrm{R}} = -m\nabla\mu, \tag{6.5}$$

where the mobility m of the Li is a function of the concentration given by

$$m = \frac{D_0}{R\vartheta}c(1-\bar{c}), \tag{6.6}$$

with D_0 a constant diffusion coefficient.

7 Governing partial differential equations. Boundary conditions

In the absence of non-inertial body forces and neglect of inertial forces, standard considerations of balance of forces, when expressed spatially in the deformed body $\mathcal{B} = \boldsymbol{\chi}(\mathrm{B})$, give that the symmetric Cauchy stress tensor $\mathbf{T}$ satisfies the force balance

$$\operatorname{div} \mathbf{T} = \mathbf{0}. \tag{7.1}$$

With $\mathcal{S}_{\mathbf{u}}$ and $\mathcal{S}_{\mathbf{t}}$ denoting complementary subsurfaces of the boundary $\partial\mathcal{B}$ of the deformed body, we consider a pair of boundary conditions in which the displacement $\mathbf{u} = \mathbf{x} - \mathbf{X}$ is specified on $\mathcal{S}_{\mathbf{u}}$ and the surface traction on $\mathcal{S}_{\mathbf{t}}$ for a time interval $t \in [0, T]$:

$$\left.\begin{aligned} \mathbf{u} &= \breve{\mathbf{u}} \quad \text{on } \mathcal{S}_{\mathbf{u}} \times [0,T], \\ \mathbf{T}\mathbf{n} &= \breve{\mathbf{t}} \quad \text{on } \mathcal{S}_{\mathbf{t}} \times [0,T]. \end{aligned}\right\} \tag{7.2}$$

Then (7.1), the constitutive equations for $\mathbf{T}$ expressed in terms of the deformation, together with (7.2) yields a boundary value problem for the displacement field $\mathbf{u}(\mathbf{x}, t)$. The field equation (7.1) and boundary conditions (7.2) are taken to hold for the anode, the electrolyte, and the SEI, with the stress $\mathbf{T}$ given by their respective constitutive equations.

We neglect diffusion of Li in the SEI. Mass balance for diffusion of Li in the anode requires that the balance equation

$$\dot{c} = -\mathrm{Div}\,(\mathbf{j}_{\mathrm{R}}) \tag{7.3}$$

hold in the anode, with the flux given by (6.5). The initial condition for c is taken as

$$c(\mathbf{X}, 0) = c_0. \tag{7.4}$$

Letting $\mathcal{S}_{\mu}$ and $\mathcal{S}_{\mathbf{j}_{\mathrm{R}}}$ denote complementary subsurfaces of the boundary $\partial\mathrm{B}$ of the reference body B describing the anode material, we consider a pair of simple boundary conditions in which the chemical potential is specified on $\mathcal{S}_{\mu}$ and the species flux on $\mathcal{S}_{\mathbf{j}_{\mathrm{R}}}$:

$$\left.\begin{aligned} \mu &= \breve{\mu} \quad \text{on } \mathcal{S}_{\mu} \times [0,T], \\ \mathbf{j}_{\mathrm{R}} \cdot \mathbf{n}_{\mathrm{R}} &= \breve{j} \quad \text{on } \mathcal{S}_{\mathbf{j}_{\mathrm{R}}} \times [0,T]. \end{aligned}\right\} \tag{7.5}$$

7.1 Numerical implementation of the theory

We have implemented our SEI growth theory, described above in Sections 4 and 5, in the implicit finite element program Abaqus/Standard (2013) by writing a a 2D axisymmetric 4-node linear isoparametric quadrilateral user element subroutine (UEL).[2] We have coupled this numerical capability for SEI growth with our previously developed user element subroutine (UEL) for simulation of lithiation and delithiation of electrode particles, Section 6. For brevity, we omit all details of our numerical implementation.

In the next two sections we report on the results from our numerical simulations for the following two case studies:

1. A study of SEI formation on the surface of a flat anode undergoing cyclic lithiation and delithiation, as in the paper of Mukhopadhyay et al. (2012).

2. A study of SEI formation on the surface of spherical and spheroidal graphite particles undergoing cyclic lithiation and delithiation.

[2] We have also implemented a 2D plane-strain 4-node linear isoparametric quadrilateral element, and a 3D 8-node linear isoparametric brick; however, we do not show any simulations using these elements in this paper.

8 SEI formation on the surface of a flat anode undergoing cyclic lithiation and delithiation

The purpose of this section is to use the novel experimental results of Mukhopadhyay et al. (2012) to calibrate the material parameters in our theory and to verify whether our theory is able to reproduce their experimental results with reasonable quantitative accuracy.

In their experiments Mukhopadhyay et al. (2012) did not continuously monitor the thickness of the SEI layer as it grows, they only reported that the thickness of the SEI layer after 811 hours of cyclic lithiation was $h \approx 100$nm. Thus, guided by the experimental results of Smith et al. (2011) who showed that the loss of Li in the battery (capacity fade) is proportional to the square root of time, we assume (as discussed previously in Section 4) that

$$h(t) = h(t_f)\sqrt{t/t_f}, \qquad \text{with} \quad t_f = 811\,\text{hours} \quad \text{and} \quad h(t_f) = 100\,\text{nm}. \tag{8.1}$$

In order to estimate the material parameters in our in-plane SEI growth model, we carried out a finite-element simulation of the experiments of Mukhopadhyay et al. (2012), which we describe below. Their physical experiment was performed on a 1 in-diameter quartz substrate, as shown schematically in Fig. 6(a). In order to minimize the computational effort, we considered a small section of the axisymmetric plate immediately adjacent to the axis of radial symmetry as our simulation domain, and meshed it with a single column of elements, as shown schematically in Fig. 6(b). The electrolyte/SEI layer was meshed with 150 elements whose constituve behavior is described by the deposition and expansion model developed in Sects. 4 and 5. The graphite layer was meshed with 40 elements whose constitutive behavior is described by the coupled deformation-diffusion theory summarized in Sect. 6. Finally, the quartz layer was meshed with 30 elements which are prescribed a simple linear isotropic elastic constitutive behavior.

In our simulations *we neglect the diffusion of Li-ions through the SEI*, which effectively means that we neglect any resistance offered by the SEI to the diffusion of Li in the graphite. Henceforth, for brevity, we will use the terms "fully delithiated" and "fully lithiated" to describe the graphite layer when it has an average normalized Li concentration of $\bar{c} = 0.05$ and $\bar{c} = 0.95$, respectively.

The boundary/initial conditions that we used in our simulations are as follows:

- **Mechanical boundary conditions**: Consistent with the radial symmetry of the problem, the nodes along the edge AD in Fig. 6(b) are constrained to have zero radial displacement. All nodes on the edge EH are constrained to remain on a straight line as defined by the nodes at points E and H. The line formed by the nodes along edge EH is free to move and rotate, *and it is from the rotation of this line with respect to its initial vertical position that we computed the curvature of the plate.*

- **Initial concentration of Li in the graphite**: The initial concentration of lithium in the graphite layer is taken as a low value of $\bar{c}_0 = 0.05$. In order to model the experimentally-observed stress generated during the chemical vapor deposition of the graphite, we use an alternative form of (6.2), viz.,

  $$J^c = 1 + \Omega(c - c_0) + J^c_0, \tag{8.2}$$

  where J^c_0 accounts for the initial strain mismatch in the graphite. This is used purely as a numerically-expedient tool for achieving a residual stress mimicking the stress developed during the chemical vapor deposition of the graphite layer on the quartz substrate in the experiments.

- **Chemical boundary conditions for the graphite**: The nodes on the edges BC, CF, and GF in Fig. 6 are prescribed to have zero outwards flux, i.e. $\breve{j} = 0$ (cf. eq. $(7.5)_2$). As mentioned above, we neglect the diffusion of Li-ions through the SEI and directly prescribe a constant flux of Li on the edge BG. Further, in order to study the effect of the lithiation/delithiation of the graphite on the process of SEI deposition and growth, in this particular geometry, we consider two separate cases:

  (a) **Simulation with lithiation/delithiation of the graphite**: In their experiments, Mukhopadhyay et al. used a charge rate (C-rate) of C/10, which in the absence of capacity fade would yield a lithiation/delithiation cycle with a duration of 10 hours. Due to the capacity fade, the duration was shorter and changed from cycle to cycle. Since we do not model capacity fade in

the graphite, we adjusted the C-rate to C/8.1, which corresponds to 50 cycles over the entire 811 hours of their experiment. The magnitude of the flux was then computed accordingly to get from the fully delithiated state to the fully lithiated state in a time $t_{\rm hc} = 8.1$ hours. That is,

$$\breve{j} = \begin{cases} -1.8 \cdot 10^{-7}\,\mathrm{mol}/(\mathrm{m}^2\mathrm{sec}) & 2n-2 \le t/t_{\rm hc} < 2n-1, \\ 1.8 \cdot 10^{-7}\,\mathrm{mol}/(\mathrm{m}^2\mathrm{sec}) & 2n-1 \le t/t_{\rm hc} < 2n, \end{cases} \tag{8.3}$$

where $n \in [1, \ldots, \mathbb{N}]$ is the cycle number. Such an idealized square-cyclic value for the boundary flux is schematcally shown in Fig. 7.

(b) **Simulation without lithiation/delithiation of the graphite**: In this case we ignored the lithiation and delithiation of the graphite and simply prescribed

$$\breve{j} = 0 \tag{8.4}$$

along the edge BG. Without any changes in Li concentration, the graphite responds as a purely elastic solid.

8.1 Material parameters

Using (5.52) in (5.53) we recall next the evolution equation for the area ratio Θ^g:

$$\dot{\Theta}^g = \begin{cases} k\left(1 - \dfrac{\Theta^g}{\Theta^g_{\max}}\right) \underbrace{(H + \mathbf{M}^e : \mathbf{S}^g - \frac{1}{2}\mathbf{E}^e : \mathbb{C}\mathbf{E}^e)}_{\mathcal{F}} & \text{if } \mathcal{F} > 0, \\ 0 & \text{otherwise.} \end{cases} \tag{8.5}$$

At this stage of research in the field, not enough is known to fully characterize the material parameters appearing in such an evolution equation. In our simulations, for pragmatic reasons, we choose a sufficiently large value of the chemical modulus H so that $H \gg (\mathbf{M}^e : \mathbf{S}^g - \frac{1}{2}\mathbf{E}^e : \mathbb{C}\mathbf{E}^e)$, and the steady state at which the evolution of Θ^g stops, occurs when $\Theta^g = \Theta^g_{\max}$. Thus, the rate at which the evolution of area growth strains occurs within the SEI is then primarily controlled by $1/(kH)$, which represents a characteristic time for the evolution of Θ^g. Specifically, we choose values of

$$H = 8 \times 10^6\,\mathrm{MJ/m^3} \quad \text{and} \quad k = 10^{-7}\,\mathrm{m^3}/(\mathrm{MJ}\cdot\mathrm{sec}), \tag{8.6}$$

so that the characteristic time is

$$1/(kH) = 1.25\,\mathrm{sec}. \tag{8.7}$$

With this choice for the parameter pair (k, H), the area swelling ratio Θ^g in a particular layer of SEI elements reaches its maximum value $\Theta^g_{\max}$, before the next layer of SEI elements is deposited according to the deposition scheme described by (8.1).

With k and H fixed at the values in (8.6) above, the rest of the material parameters for the SEI, as well as the parameters for the graphite and the quartz that we have used to fit the experiments of Mukhopadhyay et al. (2012), are summarized in Table 1.

Table 1: Material parameters for SEI, graphite, and quartz used to fit the experiments of Mukhopadhyay et al. (2012)

Layer	Parameter	Value	Source
SEI	E_{S}	$25\,\mathrm{GPa}$	Fitted
	ν_{S}	0.3	
	$\Theta^{g}_{\max}$	1.088	
Graphite	E_{G}	$100\,\mathrm{GPa}$	Qi et al. (2010)
	ν_{G}	0.3	
	Ω	$1.249 \cdot 10^{-7}\,\mathrm{m}^3/\mathrm{mol}$	
	$c_{\max}$	$2.914 \cdot 10^{4}\,\mathrm{mol}/\mathrm{m}^3$	Christensen and Newman (2006)
	D_0	$10^{-13}\,\mathrm{m}^2/\mathrm{s}$	
Quartz	E_{Q}	$72\,\mathrm{GPa}$	De Jong et al. (2000)
	ν_{Q}	0.165	

Remark. The values for E_G and Ω for graphite used here are an adaptation of the results from a density functional theory (DFT) calculations by Qi et al. (2010). In their density functional theory analysis, Qi et al. (2010) predicted a 1.2% stretch of all material fibers in the basal plane. A corresponding value for isotropic swelling which yields 1.2% stretch of *all* material fibers is $\Omega c_{\max} = 3.63 \cdot 10^{-2}$. Further, they found the stiffness in the basal-plane to vary with respect to composition, with an average of $C_{11} \sim 1047\,\mathrm{GPa}$. However, we find these DFT-based calculated values to be too high, and inconsistent with the experimental results of Mukhopadhyay et al. (2012). Accordingly, in our simulations we have chosen substantially reduced values for the stiffness E_G and the total swelling $\Omega c_{\max}$ — values which, when compared to those based on Qi et al. (2010), are lower by a factor of ten. □

8.2 Simulation results

As summarized in Section 1, Mukhopadhyay et al. (2012) interpreted their experimentally-measured curvatures in terms of a nominal stress which was calculated using Stoney's formula (1.1); cf. Fig. 3. Since our numerical simulations directly give us the results for the curvature changes, we have converted their reported stress values back to curvature values by using (1.1), the material parameters for the quartz in Table 1, and the thicknesses of the quartz and graphite layers presented in Fig. 6. Their experimental curvature versus time results are shown as a blue line in Fig. 8 (a). The corresponding curvature versus time from our finite element simulation results are also plotted in this figure as a red line. The two important experimentally-observed phenomena are clearly captured by our numerical simulations:

(i) First, there as an overall decrease of the curvature κ as a function of time — this is due to the growth of the SEI layer.

(ii) Second, overlaid on the overall decrease in curvature, there is a cyclic oscillation of the curvature — this is due to the lithiation/delithiation cycles of the graphite layer.

Highlighted in Fig. 8 (a) by blue dots are the experimental curvature measurements after a complete lithiation/delithiation cycle. These points correspond to instances when the graphite layer is essentially free of Li. These experimental curvature measurments after full lithiation/delithiation cycles are replotted in Fig. 8(b) as blue dots. In this figure we also show the results of our numerical simulations **without** the lithiation/delithiation of the graphite, that is, the case corresponding to the boundary condition (8.4); this result is shown as a red line. The drop in curvature with time in the numerical results in Fig. 8 (b) is due entirely to the growth of the SEI layer. This numerically-predicted curvature history agrees well with the experimental curvature measurements taken after full lithiation/delithiation cycles.

In in Fig. 8 (a) the experimental results show an increase in the amplitude of the cyclic oscillations of the curvature which, as noted by Mukhopadhyay et al. (2012), are consistent with an increase in the capacity of the graphite. In our simulations, we have not considered any variation in the capacity of the graphite during cycling. Thus, the amplitude of the oscillations in the stress in our simulations remain constant during cycling.

The results in Fig. 8 are extremely encouraging, they show that our theory and numerical simulation capability — with suitable choices for the material parameters — can reproduce the sophisticated experimental results of Mukhopadhyay et al. (2012) with reasonable *quantitative* accuracy.

9 SEI formation on the surface of spherical and spheroidal graphite particles undergoing cyclic lithiation and delithiation

In this section we numerically simulate SEI growth on a spherical-shaped anode particle during cyclic lithiation/delithiation, and compare the results obtained for a spherical particle against those for a particle geometry which is spheroidal rather than perfectly spherical.

Andersson et al. (2003) have reported on their measurements of SEI growth on graphite particles with an average diameter of $\approx 3\,\mu$m. In their experiments they performed two full lithiation/delithiation cycles at a C-rate of C/7. After cycling and washing of the anode, they measured an SEI thickness of $\approx 45\,$nm. Guided by the experiments of these authors, in our simulations we choose the dimensions of the graphite particles to have a diameter of $\approx 3\,\mu$m. Specifically, we consider the spherical- and spheroidal-shaped particles schematically shown in Fig. 9: the spherical particle is taken to have a radius of $1.5\,\mu$m, and the spheroidal particle to have a major axis of $2\,\mu$m and a minor axis of $1\,\mu$m. Due to the symmetries in the geometry, we mesh only one-half of the axisymmetric profile of each particle. Both particles are meshed using 7500 elements, together with an electrolyte/SEI layer which is meshed using 5000 elements — with 50 elements in the direction normal to the anode surface and 100 elements along the surface of the anode particle. The properties for the SEI are taken as those calibrated in Section 8 and listed in Table 1. However, following Christensen and Newman (2006), for an "isotropic" graphite anode we use,

$$E_G = 15\text{GPa}, \quad \nu_G = 0.3, \quad \Omega = 2.745 \cdot 10^{-6}\,\text{m}^3/\text{mol}, \quad c_{\max} = 2.914 \cdot 10^4 \text{mol}/\text{m}^3, \quad D_0 = 10^{-13}\,\text{m}^2/\text{s}. \tag{9.1}$$

Further, based on the work of Andersson et al. (2003), we prescribe the thickness of the SEI to evolve according to (cf., eq. (8.1))

$$h(t) = h(t_f)\sqrt{t/t_f}, \quad \text{with} \quad t_f = 28\,h \quad \text{and} \quad h(t_f) = 45\,\text{nm}, \tag{9.2}$$

With reference to Fig. 9, the boundary and initial conditions that we used in our simulations are as follows:

- **Mechanical boundary conditions**: Symmetry conditions are prescribed on edges BE and BD, where the nodes along BE are constrained to have zero radial displacement while the nodes along BD are constrained to have zero vertical displacement. The exterior boundary DE is taken to be traction-free.

- **Chemical initial conditions**: The initial concentration of Li in the graphite particles is taken to have a low value of $\bar{c}_0 = 0.05$.

- **Chemical boundary conditions**: In accordance with the symmetry conditions on edges BA and BC, the nodes along these edges are prescribed to have zero outwards flux, i.e. $\breve{j} = 0$. As in Sect. 8, we neglect diffusion of Li-ions through the electrolyte/SEI layer, and prescribe a constant flux of Li ions on the edge AC. We consider the following two cases:

  (a) **Simulations with lithiation/delithiation of the graphite particle**: First, we account for the lithiation and delithiation of the graphite anode particle, concurrently with SEI growth, by considering a non-zero value of the flux prescribed on the anode edge AC. Specifically, consistent with the experiments of Andersson et al. (2003) we prescribe a flux according to a C-rate of C/7;

viz., a flux which takes the particle from a fully delithiated state into a fully lithiated state in 7 hours and vice verse:

$$\breve{j} = \begin{cases} -5.20 \cdot 10^{-7}\,\mathrm{mol/(m^2 sec)} & 2n-2 \le t/t_{\mathrm{hc}} < 2n-1 \\ 5.20 \cdot 10^{-7}\,\mathrm{mol/(m^2 sec)} & 2n-1 \le t/t_{\mathrm{hc}} < 2n \end{cases} \tag{9.3}$$

for the spherical particle, and

$$\breve{j} = \begin{cases} -4.26 \cdot 10^{-7}\,\mathrm{mol/(m^2 sec)} & 2n-2 \le t/t_{\mathrm{hc}} < 2n-1 \\ 4.26 \cdot 10^{-7}\,\mathrm{mol/(m^2 sec)} & 2n-1 \le t/t_{\mathrm{hc}} < 2n \end{cases} \tag{9.4}$$

for the spheroidal particle, with $t_{\mathrm{hc}} = 7$ hours. The difference in the prescribed fluxes for the spherical and spheroidal particles is due to their different surface-area-to-volume ratios. As in the experiments of Andersson et al., in our simulations we carry out two full lithiation/delithiation cycles.

(b) **Simulations without lithiation/delithiation of the graphite particle**: In order to study the effect of graphite swelling on the stresses in the SEI layer we have also performed simulations with no lithiation of the graphite by simply prescribing a zero normal flux along the edge AC,

$$\breve{j} = 0.$$

We have applied the same SEI growth rates in order to have results comparable to the simulations with lithiation/delithiation.

The results from the numerical simulations for the spherical and spheroidal-shaped particles are discussed in the next two subsections.

9.1 Simulation results for SEI growth on a spherical anode particle

As described above, the simulations were run for two complete cycles of lithiation and delithiation of the anode particle, with simultaneous deposition and expansion of the SEI. The two full cycles of lithiation/delithiation are of course equivalent to four half-cycles — each half-cycle consisting of either fully lithiating or fully delithiating the anode particle. Figs. 10(a) and (b) show plots of the variation of the hoop stress $T_{\theta\theta} = \mathbf{e}_\theta \cdot \mathbf{T}\mathbf{e}_\theta$ (in a cylindrical coordinate system, cf. Fig. 10) within the SEI layer *at the north-pole of the particle*, as a function of the outward distance from the surface of the anode; cf. the schematic on the left of Fig. 10(a). These figures thus show the variation of the "hoop-stress" in the SEI as a function of the outward distance from the surface of the anode.

Fig. 10(a) compares the result for the hoop stress variation in the SEI for a simulation with two complete (or four half-cycles) of lithiation/delithiation of the graphite (solid line), against the result for a simulation in which the graphite is not lithiated (dashed line). At the end of the two full-cycles the graphite is delithiated, as it is in the case when the graphite is never lithiated. In the case of no lithiation of the graphite the hoop stress in the SEI layer is almost uniform at a value of approximately -1.5 GPa, whereas with cyclic lithiation the hoop stress varies in the approximate range -2.3 GPa to -1.5 GPa across the thickness of the SEI layer.

The variation in hoop stress within the SEI thickness for the case of cyclic lithiation arises due to the fact that as the SEI deposition and growth is occurring, the underlying graphite is also undergoing relatively large volumetric changes due to the intercalation of Li. This result is easily understood using the schematic shown in Fig. 11. Consider a fully lithiated particle shown in Fig. 11(a) onto which an SEI layer forms, Fig. 11(b). The SEI layer which forms will be in compression due to the inherent growth hoop stress which arises during the process of SEI expansion. Once the particle delithiates, see Fig. 11(c), the SEI layer will develop *higher* compressive stresses due to volumetric shrinking of the graphite particle onto which the SEI layer is attached. The regions of the SEI in Fig. 10(a) which have the largest compressive stresses of ~ -2.3 GPa thus correspond to layers of SEI which were formed when the particle was fully lithiated.

To further illustrate the importance of accounting for stress generation due to both the SEI growth and the lithiation/delithiation of the underlying graphite particle, Fig. 10(b) shows the results of the simulation with cyclic lithiation of the graphite at two different times: (i) at the end of 4 half-cycles when the anode

is delithiated (solid line), and (ii) at the end of 3 half-cycles when the anode is fully lithiated (dashed line). As expected, when the graphite is fully lithiated, the overall hoop stress profile through the thickness of the SEI exhibits lower levels of compressive hoop stress than at the state when it is fully delithiated, since some of the compressive stress is relieved by the volumetric swelling of the graphite anode when it is lithiated.

Of significant interest for judging the tendency for the SEI layer to delaminate from the anode particle is the normal component of the traction, $T_n = \mathbf{n} \cdot \mathbf{Tn}$, where $\mathbf{n}$ is the outward unit normal to the anode/SEI interface; cf. schematic on the left of Fig. 10(c). Figs. 10(c) and (d) show the variation of T_n at the anode/SEI interface as a function of the normalized distance along the circumference of the particle, starting from the north-pole of the particle. As before, Fig. 10(c) shows the result from a simulation with cyclic lithiation/delithiation of the graphite (solid line) versus the result from a simulation in which the graphite is not lithiated (dashed line). The normal stress profiles in this figure are computed at the end of four half-cycles when the graphite is equally devoid of Li in both simulations. Note that the addition of cyclic lithiation/delithiation of the graphite leads to the development of larger tensile normal stress T_n at the anode/SEI interface. The larger value of T_n in the simulation with cyclic lithiation of the graphite is consistent with the observation of the larger compressive hoop stress in the SEI layer for the same simulation, cf. Fig. 10(a).

Finally, Fig. 10(d) shows the results for T_n for the simulation with cyclic lithiation of the graphite at two different times: (i) at the end of 4 half-cycles when the anode is delithiatated (solid line), and (ii) at the end of 3 half-cycle when the anode is fully lithiated (dashed line). When the particle is lithiated (dashed line) the normal interface stress is $\sim$ 55 MPa, whereas at when the particle is delithiated (solid line) the normal stress is $\sim$ 115 MPa. This illustrates the contribution of the delithiation of graphite anode to the formation of additional normal stress along the anode/SEI interface.

9.2 Simulation results for SEI growth on a spheroidal anode particle

In this section we present the results of our simulations for a spheroidal graphite particle and compare (i) the hoop stress distribution in the SEI layer, as well as (ii) the normal stress distribution at the anode/SEI interface, against the corresponding results for a spherical particle. The results in this section are presented in the same fashion as was done in Sect. 9.1 for the case of a spherical particle.

Figs. 12(a) and (b) show plots of the variation of the hoop stress at the north-pole of the spheroidal particle in the SEI layer as a function of the distance from the surface of the anode. These results are similar to those in Figs. 10(a) and (b) for a spherical particle.

Figs. 12(c) and (d) show the normal traction T_n at the anode/SEI interface as a function of the normalized distance along the circumference of the particle. These results *differ significantly* from those obtained using a spherical particle; compare with Figs. 10(c) and (d). In the spheroidal particle the normal traction along the anode/SEI interface in the vicinity of the north-pole of the particle, is substantially higher than the normal traction in a spherical particle. Focusing on the normal traction after 4 half-cycles — when the particle is fully delithiated — we see that the normal traction for the spheroidal particle, Fig. 12(d) (solid line), reaches a maximum value of $\sim$ 320 MPa at the north-pole. In contrast, the normal traction in the sphere, Fig. 10(d) (solid line), reaches a maximum value of $\sim$ 120 MPa, which is constant along the circumference of the particle.

The substantial increase in normal tensile traction at the anode/SEI interface for a spheroidal (non-spherical) particle — as compared to a spherical particle — is important in developing a more complete understanding of the role of particle shape in increasing (or decreasing) the potential for delamination of a SEI layer from an anode particle.

Remark. In order to determine whether the SEI delaminates from the anode, the maximum calculated value of T_n must be compared with the cohesive strength of the interface. However, to the best of our knowledge, measurements of cohesive strengths of SEI/anode interfaces have not been reported in the literature. Still, examining the evolution of the normal stress T_n at the interface provides some insight as to when the SEI might delaminate. Fig. 13 shows the evolution of T_n near the north pole of the spheroidal particle for two full lithiation/delithiation cycles. In the first half-cycle of lithiation the normal stress T_n increases, while in the second half-cycle of lithiation T_n decreases. However T_n increases during both delithiation half-cycles — which is to be expected because the graphite shrinks away from the SEI layer during delithiation. Thus,

once an SEI layer has been formed, delamination of this layer from the anode is most likeley to occur during *delithiation.*

□

10 Concluding Remarks

We have formulated a new continuum-mechanical theory and a finite-element-based capability for the simulation of growth of a solid electrolyte interphase layer at an anode particle in a Li-ion battery. Our simulation capability accounts for the stress-generation due to the growth of a SEI layer, as well as the cyclic stresses that are generated due to the lithiation and delithiation of the anode particle.

We have calibrated the material parameters in our theory by using available data from the literature, and by using results from the substrate curvature experiments of Mukhopadhyay et al. (2012). The results that we have presented in Section 8 are extremely encouraging; they show that our theory and numerical simulation capability — with suitable choices for the material parameters — can reproduce the novel experimental results of Mukhopadhyay et al. (2012) with reasonable *quantitative* accuracy.

The calibrated theory has been used to simulate SEI growth on a spherical and a spheroidal graphite anode particle. Our simulations show that large non-uniform compressive hoop stresses are generated within the SEI due to both the growth of the SEI and the lithiation/delithiation of the anode particle. Our study shows that SEI layers which are formed on the anode while it is in an expanded/lithiated state will develop higher compressive hoop stresses once the anode is subsequently delithiated. These findings are especially important since they in turn affect the large normal tensile tractions which develop along the anode/SEI interface — tractions which can lead to the delamination-type failure of the SEI and thus to accelerated capacity fade. Our study of spheroidal versus spherical particles shows that spheroidal particles develop much larger (order 3 times larger) normal tractions at certain points at the anode/SEI interface than spherical particles do. As such, spheroidal particles are at a higher risk for potential delamination failure of the SEI.

Our work presents a first step in the modeling of SEI growth at active anode particles, and carrying out a detailed stress analysis of the process. Much remains to be done; some important items that need attention in the future include:

- The square-root of time growth for the thickening of the SEI in our model is something that has been prescribed a-priori. In a more complete future theory the square-root of time growth might be the outcome of more completely modeled diffusion-limited chemical reaction processes which involve the electrolyte, electrons, and the resulting SEI (cf., e.g., Pinson and Bazant, 2013).
- Diffusion of Li through the SEI needs to be accounted for.
- Effects of anisotropic elasticity and anisotropic diffusion in the anode particles need to be accounted for.
- Arbitrary three-dimensional particle shapes need to be studied.
- SEI growth on other types of anode particles, such as those made from silicon — which exhibits significantly larger volume changes — needs to be studied.

Finally, there is a pressing need for the direct experimental measurement of the material properies of the anode particles, the SEI layers, and the SEI/anode interfaces. This statement regarding experimental measurement of material properies is true also for all other microscopic (and macrscopic) components of Li-ion batteries.

Acknowledgements

Support from NSF (CMMI Award No. 1063626) is gratefully acknowledged.

References

Abaqus/Standard, 2013. SIMULIA, Providence, RI.

Anand, L., 1979. On H. Hencky's approximate strain-energy function for moderate deformations. ASME Journal of Applied Mechanics 46, 78–82.

Anand, L., 1986. Moderate deformations in extension-torsion of incompressible isotropic elastic materials. Journal of the Mechanics and Physics of Solids 34, 293-304.

Anand, L., Su, C., 2005. A theory for amorphous viscoplastic materials undergoing finite deformations, with application to metallic glasses. Journal of the Mechanics and Physics of Solids 53, 1362–1396.

Andersson, A.M., Henningson, A., Siegbahn, H., Jansson, U., Edström, K., 2008. Electrochemically lithiated graphite characterized by photoelectron spectroscopy. Journal of Power Sources 119-121, 522-527.

Barré, A., Deguilhem, B., Grolleau, S., Geŕare, M., 2013. A review on lithium-ion battery aging mechanisms and estimations for automotive applications. Journal of Power Sources 241, 680-689.

Christensen, J., Newman, J., 2006. Stress generation and fracture in lithium insertion materials. Journal of Solid State Electrochemistry 10, 293-319.

Di Leo, C.V., Rejovitzky, E., Anand, L., 2014.A Cahn-Hilliard-type phase-field theory for species diffusion coupled with large elastic deformations: application to phase-separating Li-ion electrode materials. Journal of the Mechanics and Physics of Solids 70, 1-29.

De Jong, B.H.W.S., Beerkens, R.G.C., van Nijnatten, P.A., Le Bourhis, E., 2000. Glass, 1. Fundamentals. Ullmann's Encyclopedia of Industrial Chemistry. John Wiley & Sons, Ltd.

Gurtin, M.E., Fried, E., Anand, L., 2010. The Mechanics and Thermodynamics of Continua. Cambridge University Press, Cambridge.

Kröner, E., 1960. Allgemeine kontinuumstheorie der versetzungen und eigenspannungen. Archive for Rational Mechanics and Analysis 4, 273-334.

Kuhl, E., 2014. Growing matter: a review of growth in living systems. Journal of the Mechanical Behavior of Biomedical Materials 29, 529-543.

Lee, E.H., 1969. Elastic plastic deformation at finite strain. ASME Journal of Applied Mechanics 36, 1–6.

Lee, M.L., Lee J.Y., Shim, H., Lee, J.K., Park, J., 2007. SEI Layer Formation on Amorphous Si Thin Electrode during Precycling. Journal of The Electrochemical Society 154, A515-A519.

Loeffel, K., Anand, L., 2011. A chemo-thermo-mechanically coupled theory for elastic-viscoplastic deformation, diffusion, and volumetric swelling due to a chemical reaction. International Journal of Plasticity 27, 1409–1431.

Mukhopadyay, A., Tokranov, A., Xiao, X., Sheldon, B.W., 2012. Stress development due to surface processes in graphite electrodes for Li-ion batteries: A first report. Electrochimica Acta 66, 28-37.

Pinson, M.B., Bazant, M.Z., 2013. Theory of SEI Formation in Rechargeable Batteries: Capacity Fade, Accelerated Aging and Lifetime Prediction. Journal of The Electrochemical Society 160, A243-A250.

Qi, Y., Guo, H, Hector, L.G., Timmons, A., 2010. Threefold Increase in the Young's Modulus of Graphite Negative Electrode during Lithium Intercalation. Journal of The Electrochemical Society 157, A558-A566.

Smith, A.J., Burns, J.C., Xiong, D., Dahn, J.R., 2011. Interpreting high precision coulometry results on Li-ion cells. Journal of The Electrochemical Society 158, A1136-A1142.

Stoney, G.G., 1909. The tension of metallic films deposited by electrolysis. Proceeding of the Royal Society A 82, 172-175.

Tokranov, A., Sheldon, B.W., Lu, P., Xiao, X., Mukhopadhyay, A., 2014. The Origin of Stress in the Solid Electrolyte Interphase on Carbon Electrodes for Li Ion Batteries. Journal of the Electrochemical Society, 161, A58-A65.

Verma, P., Maire, P., Novák, P., 2010. A review of the features and analyses of the solid electrolyte interphase in Li-ion batteries. Electrochemica Acta 55, 6332-6341.

Vetter, J., Novák, P., Wagner, M.R., Veit, C., Möller, K.-C., Besenhard, J.O., Winter, M., Wohlfahrt-Mehrens, M., Vogler, C., Hammouche, A., 2005. Ageing mechanisms in lithium-ion batteries. Journal of Power Sources 147, 269-281.

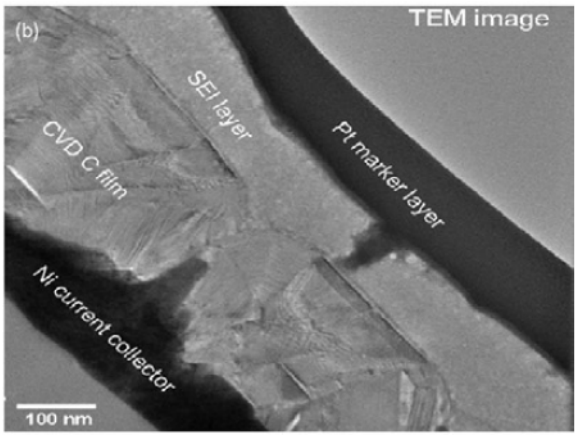

Figure 1: TEM micrograph of a SEI layer on a graphite anode. From Mukhopadhyay et al. (2012).

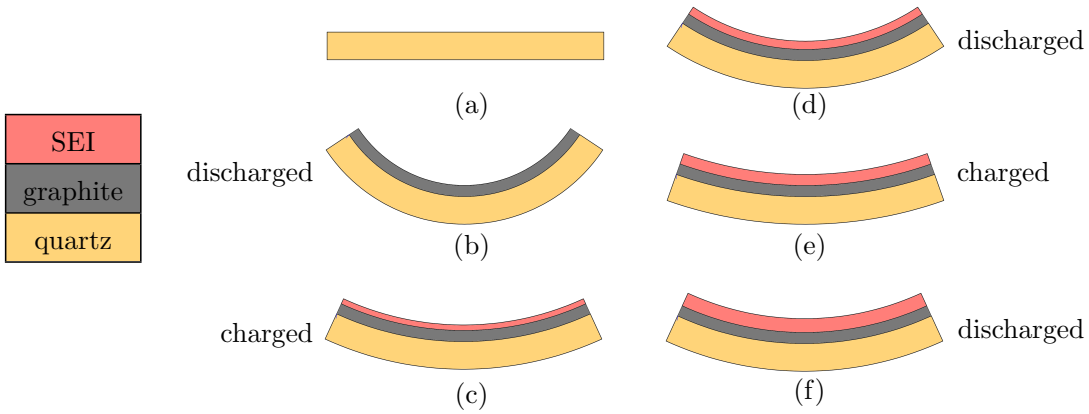

Figure 2: A schematic of the observed plate-curvature changes in the experiments of Mukhopadhyay et al. (2012): (a) the initially straight plate; (b) the curved plate after carbon deposition; (c) the curved plate, with the charged graphite at the end of the first half-cycle; (d) the curved plate at the end of the first charging/discharging cycle; (e) the curved plate, charged graphite after one and a half cycles; and (f) the curved plate, discharged at the end of two cycles.

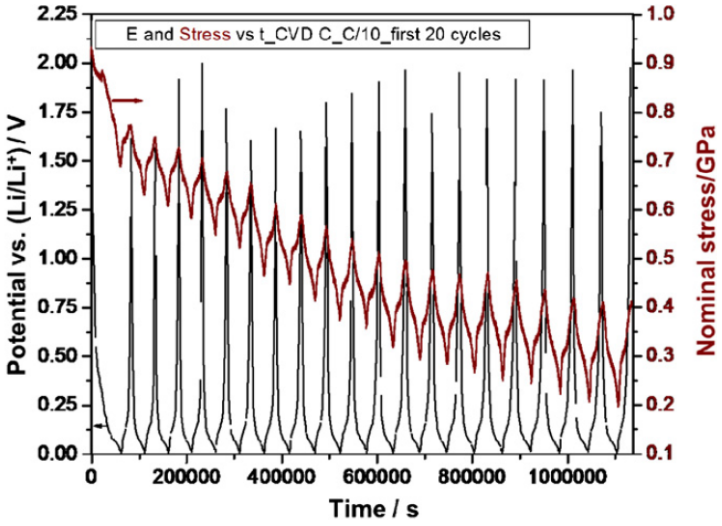

Figure 3: Variation of electrical potential and nominal stress with time for the first 20 cycles of lithiation and delithiation, as reported by Mukhopadhyay et al. (2012).

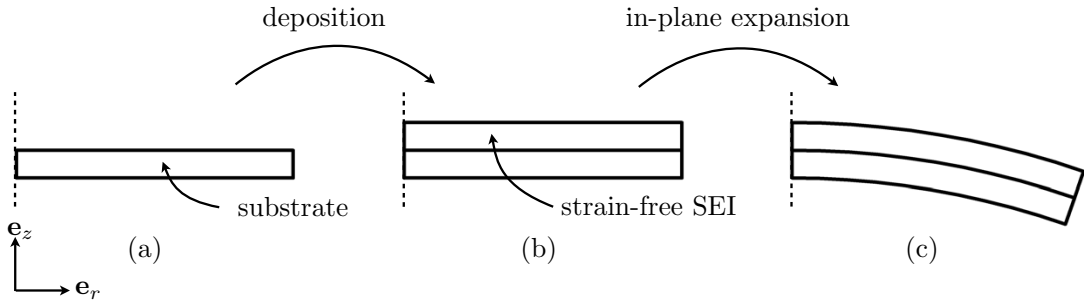

Figure 4: Idealization of SEI growth as a two-step process: (i) A "deposition" process in the direction normal to the substrate, from (a) to (b), which involves the addition of mass to the system to create a "strain-free" SEI layer. (ii) The "in-plane expansion" of the newly-deposited SEI layer, from (b) to (c).

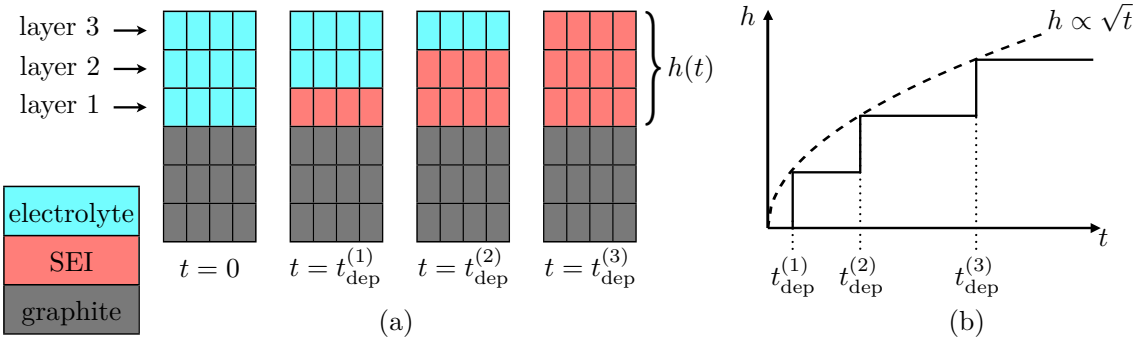

Figure 5: Schematic of the numerical simulation scheme for the deposition of an SEI layer.

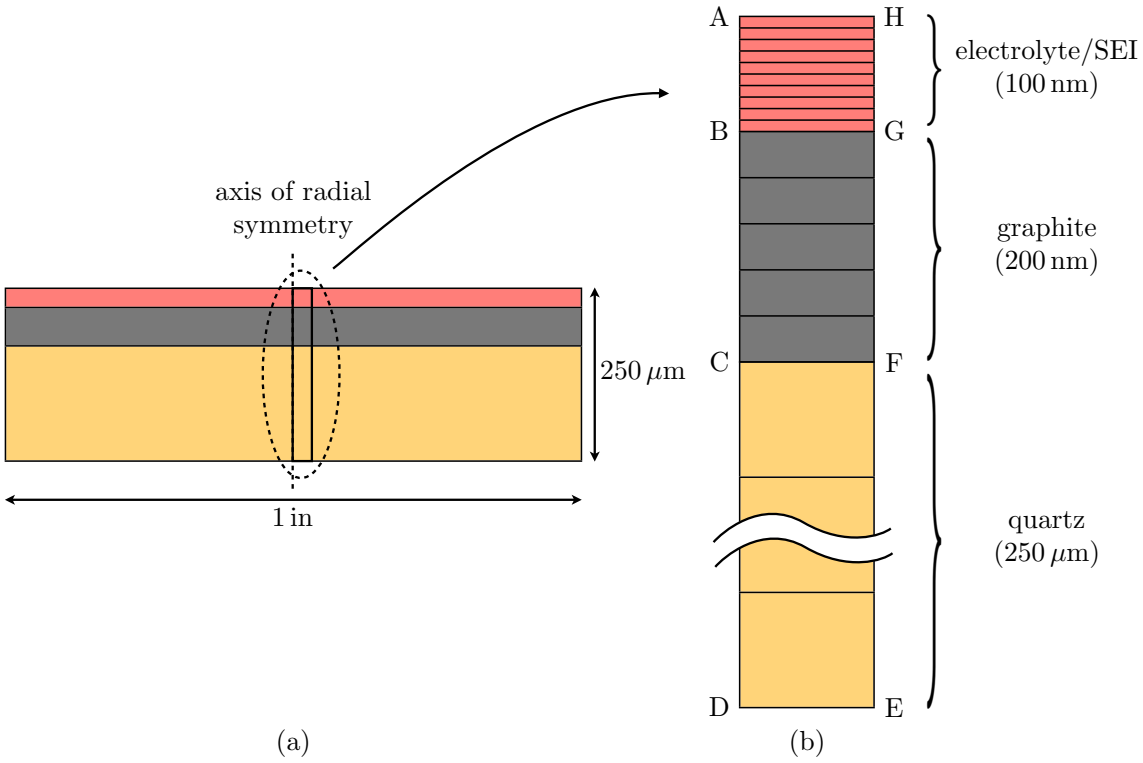

Figure 6: Plate geometry and a schematic of the single-column finite element mesh used in the simulations.

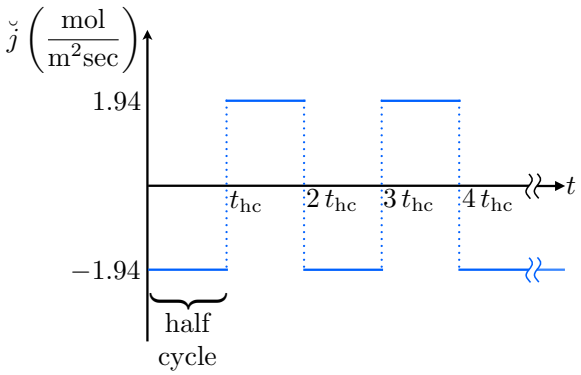

Figure 7: Schematic of the prescribed flux used in simulating galvanostatic charging/discharging. Here t_{hc} denotes the time for a half cycle of charging/discharging.

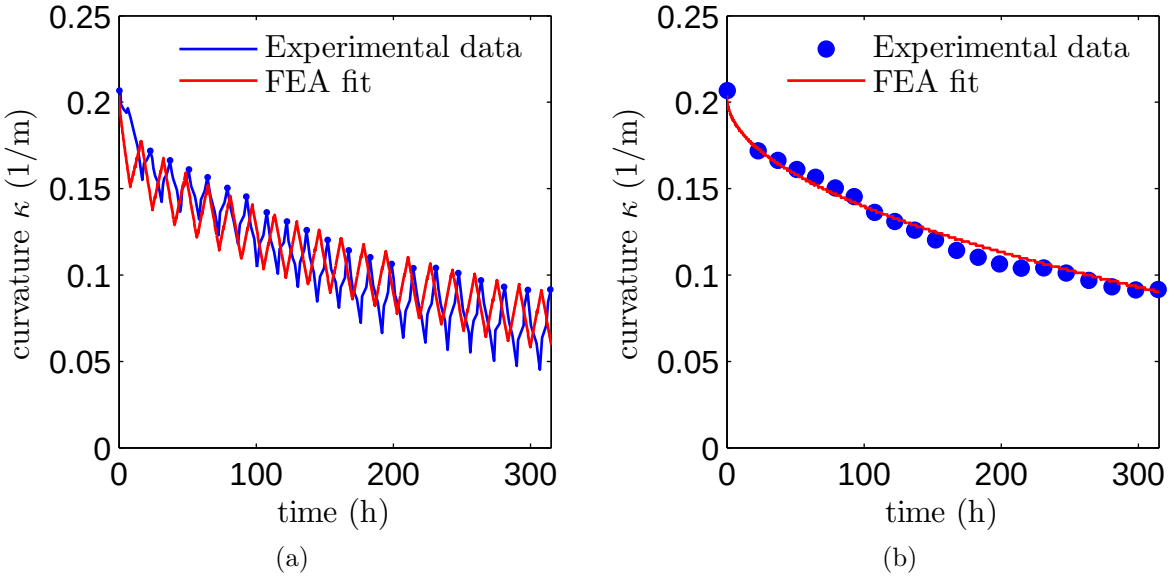

Figure 8: Experimental curvature versus time data of Mukhopadhyay et al. (2012) compared with corresponding results from finite element simulation: (a) Experimental data and simulations including lithiation/delithiation of the graphite layer. (b) Experimental data for curvatures measured only at the end of a complete lithiation/delithiation cycle compared against a numerical simulation without lithiation of the graphite.

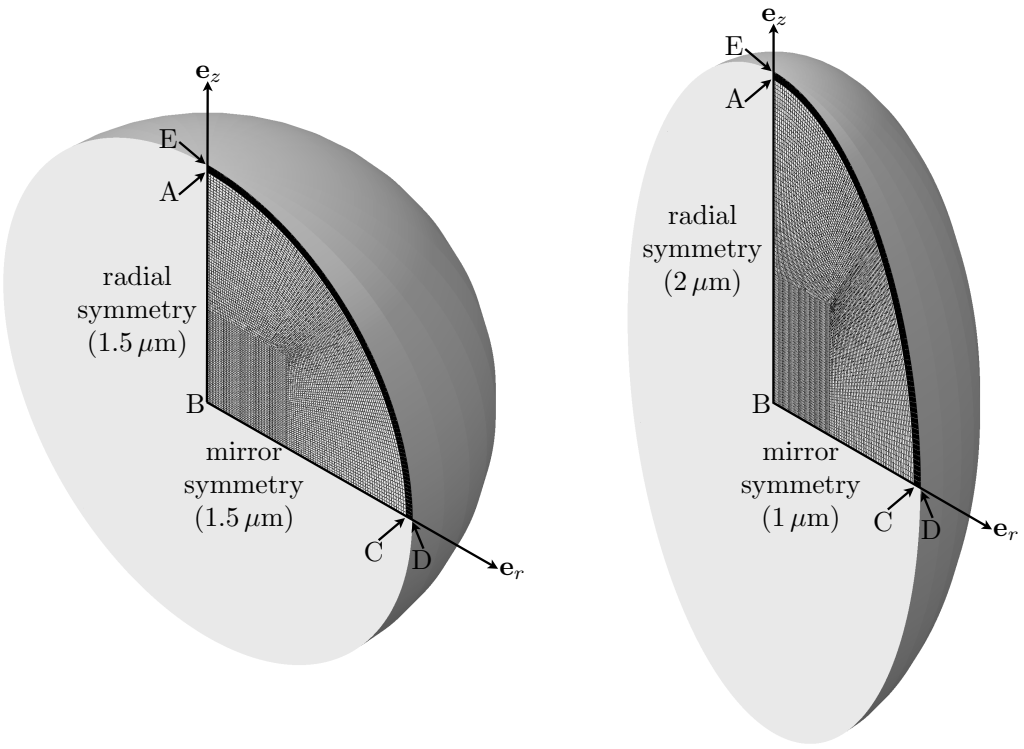

Figure 9: Geometry and finite-element mesh of the spherical and spheroidal particles used in the simulations. Due to the symmetry of the problem, only a quarter of the cross-section is meshed with axisymmetric elements.

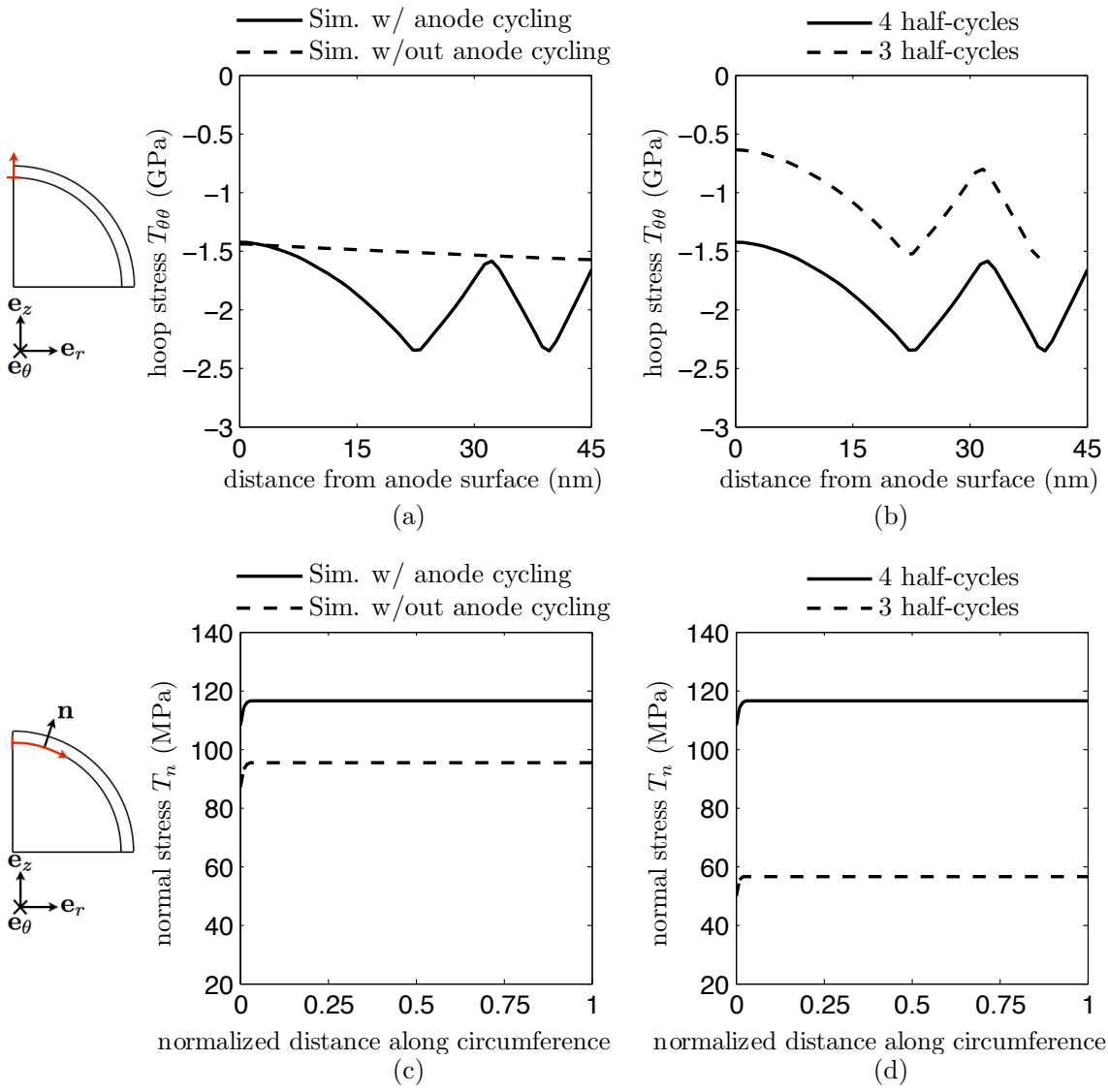

Figure 10: Simulation results for a spherical anode particle: (a) and (b) show the hoop stress $T_{\theta\theta}$ in the SEI layer as a function of the distance from the anode surface. (c) and (d) show the normal stress T_n at the anode/SEI interface as a function of the normalized distance along the circumference of the interface. (a) and (c) show results after 4 half-cycles (two full-cycles) for simulations including the cyclic lithiation/delithiation of the anode (solid lines) and for simulations without lithiation of the graphite anode (dashed lines). (b) and (d) show simulations with cycling of the anode after 3 half-cycles (dashed lines) when the graphite is lithiated and after 4 half-cycles (solid lines) when the graphite is delithiated.

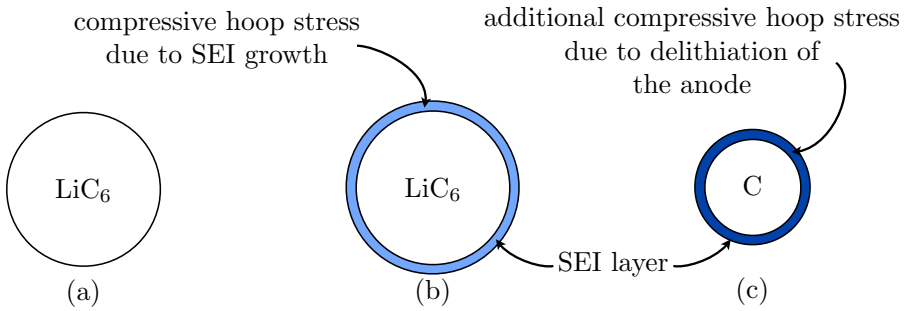

Figure 11: Schematic of SEI growth on a lithiated graphite anode followed by delithiation of the anode. The development of a compressive growth hoop stress, (a) to (b), is followed by further compression of the SEI layer due to delithiation of the graphite, (b) to (c).

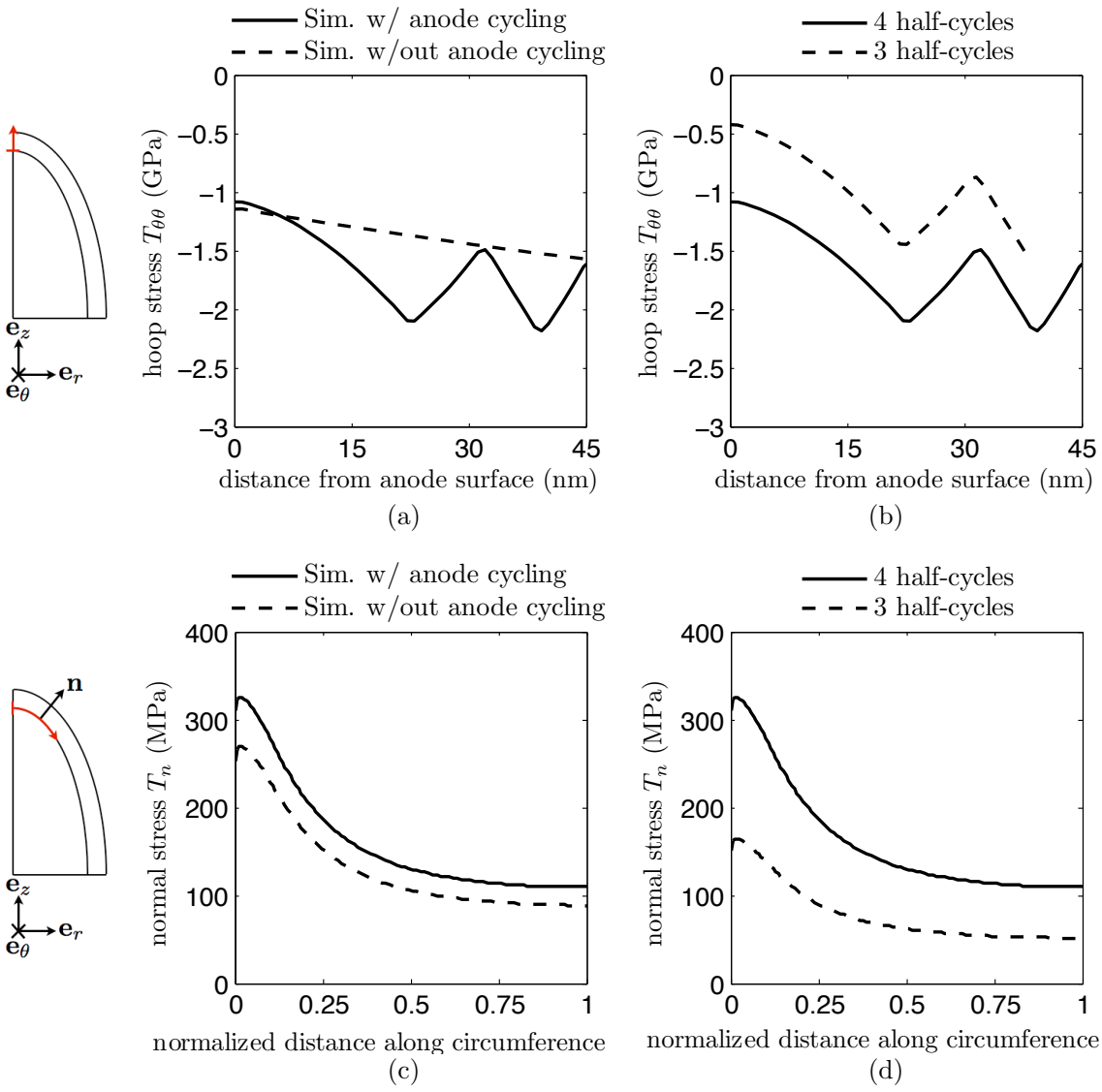

Figure 12: Simulation results for a spheroidal anode particle: (a) and (b) show the hoop stress $T_{\theta\theta}$ in the SEI layer as a function of the distance from the anode surface. (c) and (d) show the normal stress T_n at the anode/SEI interface as a function of the normalized distance along the circumference of the interface. (a) and (c) show results after 4 half-cycles for simulations including the cyclic lithiation/delithiation of the anode (solid lines) and for simulations without lithiation of the graphite anode (dashed lines). (b) and (d) show simulations with cycling of the anode after 3 half-cycles (dashed lines) when the graphite is lithiated and after 4 half-cycles (solid lines) when the graphite is delithiated.

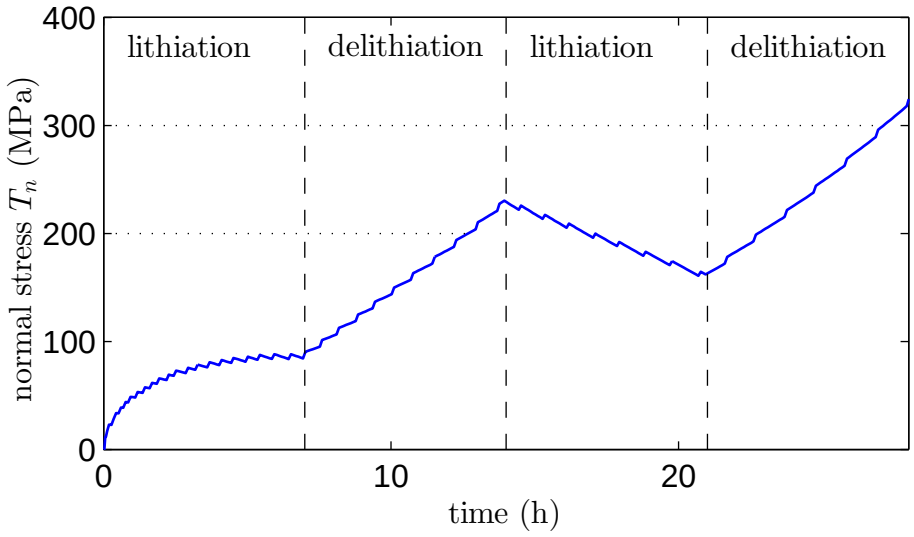

Figure 13: Variation of the normal interface traction T_n near the north pole of the spheroidal particle versus time.